Computational Materials Science 268 (2026) 114648

Contents lists available at ScienceDirect

Computational Materials Science

journal homepage: www.elsevier.com/locate/commatsci

Full length article

Thermal transport properties of diamond and hard carbon allotrope using machine-learning driven atomistic simulations

Neha Rajput, Nidheesh Virakante, Hardik L. Kagdada, Ankit Jain *

Department of Mechanical Engineering, IIT Bombay, Mumbai, 400076, India

ARTICLE INFO

Dataset link: FAU_Dataset (Original data)

Keywords:
Hard carbon
Molecular dynamics
Neuroevolution potential
GPUMD
Thermal conductivity

ABSTRACT

Hard carbons (HCs) are promising materials for energy storage applications, but their thermal transport properties remain largely unexplored. We investigate the thermal conductivity of HCs using equilibrium molecular dynamics (EMD) simulations with the machine-learning based neuroevolution potential (NEP). The localized optical phonons with small group velocities in the considered crystalline HC result in amorphous like behaviour in heat current autocorraltion function (HCACF), leading to lower thermal conductivity than diamond. Moreover, the introduction of structural disorder in crystalline HC reduces the thermal conductivity further due to localized transformation of carbon atoms from sp^2 to sp hybridization. The present work validates the NEP for carbon-based materials and provides the correlation of structural disorder and hybridization of carbon atoms with the thermal conductivity.

1. Introduction

Carbon-based materials play a vital role in energy storage systems such as lithium-, sodium-, and potassium-ion batteries. In lithium-ion batteries, graphite is commonly used as the anode material as it can accommodate intercalated lithium ions, and is cost-effective [1]. However, graphite is unsuitable for sodium- and potassium-ion batteries since the larger atomic sizes of sodium and potassium prevent effective intercalation [2,3]. As an alternative, HCs, which possess a disordered arrangement of graphitic layers, with both open and closed pores, are being extensively explored as anode materials for these systems. The porous structure of HCs enables the storage of larger atoms [4–10]. During battery charging and discharging, the intercalation and deintercalation of ions induce mechanical and thermal stresses inside the anode. Consequently, understanding of thermal transport properties of HCs is crucial for the design of efficient and stable sodium-/potassium-ion batteries. However, despite extensive research on the chemical/storage performance of HCs as battery anode materials, the thermal transport properties of HCs remain largely unexplored.

The thermal transport properties of carbon-based materials have been extensively studied in the literature for both crystalline forms (diamond, graphite, etc.) and disordered forms (amorphous, foams, aerogels, etc.). The thermal conductivity of crystalline carbons typically lies in the range of 1000–4000 W/m-K [11–14]. For disordered forms, due to lack of long-range order and reduced density, the values are two to four orders of magnitude lower, typically in the range of 0.01–10 W/m-K [15–18]. Although HCs are often classified as crystalline [19], they possess large unit cells with nearly 100% sp^2 hybridization, lack symmetry owing to structural disorders, and have low densities (less than 1 g/cm^3) [20–25]. Further, the atomic arrangements in HCs are amorphous-like; suggesting that their thermal properties may differ significantly from that of crystalline materials. Experimentally, Smontara et al. investigated thermal properties of fullerene-derived HCs and reported a 300 K thermal conductivity of 5.5 W/m-K [26]. However, considering that this reported thermal conductivity is already disorder-like to start with, it is unclear if the thermal conductivity will undergo any changes (with disorder) during the charging/discharging of the battery.

To address this, in this study, we employ molecular dynamics simulations to investigate thermal transport properties in crystalline and disordered phases of HCs. In particular, we studied thermal transport in FAU (also known as faujasite, a zeolite templated carbon material produced using faujasite-type zeolite Y as a nanotemplate [27–29]) using EMD. We find that the thermal conductivity of FAU is only 5.43 W/m-K at 300 K compared to more than 2348 W/m-K for diamond. Our modal phonon analysis suggests that this is owing to reduced phonon group velocities, stronger anharmonicity, and larger phonon scattering phase space. Further, when we convert this crystalline phase of FAU to an amorphous phase, via computational heating and quenching, the thermal conductivity reduces to less than 1.5 W/m-K.

* Corresponding author.
E-mail address: a_jain@iitb.ac.in (A. Jain).

https://doi.org/10.1016/j.commatsci.2026.114648
Received 10 January 2026; Received in revised form 6 March 2026; Accepted 14 March 2026
Available online 23 March 2026

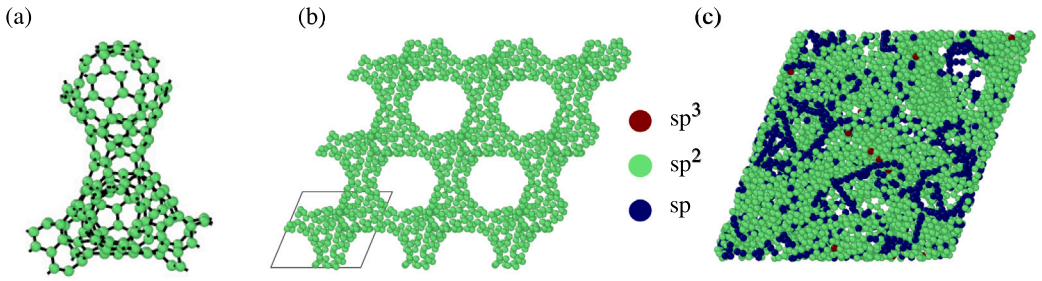

Fig. 1. (a) Schematic of closed-strut unit cell of FAU, (b) Schematic of the 3 × 3 × 3 supercell of FAU with the unit cell highlighted, and (c) Amorphous structure obtained from FAU containing 75.29% sp^2, 24.26% sp, and 0.44% sp^3.

2. Methodology

The crystal structure of FAU is obtained via the zeolite-templating method described in Ref. [28]. The unit cell of FAU consists of 176 atoms and belongs to the triclinic crystal family. The schematics of closed-strut unit cell and the 3 × 3 × 3 supercell of FAU (with highlighted unit cell) are presented in Fig. 1(a) and (b), respectively. This considered variant has a density of 0.88 g/cm^3 (compared to 3.53 g/cm^3 in diamond) with 100% sp^2 hybridization (compared to 100% sp^3 in diamond).

The EMD simulations are performed using the GPUMD (Graphics Processing Units Molecular Dynamics) package [30] with NEP. NEP is a general-purpose machine-learning potential, and the version that we used (NEP4) is trained with the following hyperparameters: cutoff 7 4; n_max 12 8; basis_size 16 12; l_max 4 2 1; neuron 100; lambda_1 0; lambda_e 1; lambda_v 0.1; batch 8000; population 100; generation 2e6 (see Ref. [31] for further details). The potential is trained on the GAP-20 dataset, which contains energies/forces computed using density functional theory (DFT) for diamond, graphite, fullerenes, carbon nanotubes, and amorphous carbon [32]. The thermal conductivity, κ, is calculated using the EMD method, based on the Green-Kubo formulism:

$$\kappa = \frac{1}{3Vk_BT^2}\int_0^\infty \langle \mathbf{J}(t)\cdot\mathbf{J}(0)\rangle\, dt, \tag{1}$$

where $\mathbf{J}$ is the heat current, $\langle \mathbf{J}(t)\cdot\mathbf{J}(0)\rangle$ is the HCACF, the angular bracket indicates the ensemble average (equal to the time average in EMD), V is system volume, k_B is the Boltzmann constant, and T is the temperature. $\mathbf{J}(t)$ and $\mathbf{J}(0)$ denote the total heat current of the system at two time instants separated by a time interval t [33,34]. The expression for the heat current ($\mathbf{J}$) in molecular dynamics simulations can be derived using the force and energy relations for each atom. The total heat current at an instant is given by the sum of the potential ($\mathbf{J}^{\mathrm{p}}$) and kinetic ($\mathbf{J}^{\mathrm{k}}$) parts of the heat current.

$$\mathbf{J} = \mathbf{J}^{\mathrm{p}} + \mathbf{J}^{\mathrm{k}} = \sum_i \mathbf{J}_i^{\mathrm{p}} + \sum_i \mathbf{J}_i^{\mathrm{k}}, \tag{2}$$

The kinetic contribution $\mathbf{J}^{\mathrm{k}}$ arises from the motion of atoms carrying their individual energies and is given by:

$$\mathbf{J}_i^{\mathrm{k}} = \mathbf{v}_i E_i, \tag{3}$$

where $\mathbf{v_i}$, $\mathbf{E_i}$ are velocity and total energy of atom i. The potential contribution $\mathbf{J}^{\mathrm{p}}$ originates from interatomic interactions and energy transfer through atomic forces and is defined as:

$$\mathbf{J}_i^{\mathrm{p}} = -\frac{1}{2}\sum_{j\neq i}\mathbf{r}_{ij}\left(\frac{\partial U_i}{\partial \mathbf{r}_{ij}}\cdot\mathbf{v}_j - \frac{\partial U_j}{\partial \mathbf{r}_{ji}}\cdot\mathbf{v}_i\right), \tag{4}$$

where $\mathbf{r}_{ij}$ is the relative position vector between atoms i and j, and U_i and U_j are the potential energies of the respective atoms. The potential part of the heat current can also be expressed in equivalent forms:

$$\mathbf{J}_i^{\mathrm{p}} = -\sum_{j\neq i}\mathbf{r}_{ij}\left(\frac{\partial U_i}{\partial \mathbf{r}_{ij}}\cdot\mathbf{v}_j\right), \tag{5}$$

or equivalently,

$$\mathbf{J}_i^{\mathrm{p}} = \sum_{j\neq i}\mathbf{r}_{ij}\left(\frac{\partial U_j}{\partial \mathbf{r}_{ji}}\cdot\mathbf{v}_i\right). \tag{6}$$

These expressions describe how energy is transferred microscopically through atomic motion and interatomic forces, forming the basis for evaluating thermal conductivity via the Green–Kubo formalism.

We simulated FAU and diamond with periodic boundary conditions with a timestep of 1 fs. All results are obtained for isotopically pure samples. For FAU, we employed a 3 × 3 × 3 simulation cell with a total of 4752 atoms, while for diamond we used 8 × 8 × 8 cell with 4096 atoms. These simulation cell sizes are verified to result in size-independent results. The change in obtained thermal conductivity is less than 5% on increasing the size to 4 × 4 × 4 for FAU and 9 × 9 × 9 for diamond. For equilibrating the structures, we employ NPT ensemble at 0 GPa and 300 K for 2 ps, followed by NVE ensemble for another 2 ps. After equilibration, the production run is carried out using the NVE ensemble for 6 ps, during which the heat flux is recorded every five timesteps. The reported thermal conductivity is obtained by averaging over 25 seeds with random initial velocity using a correlation length of 400 ps. On varying the number of seeds between 15 and 40, the changes in thermal conductivity remain at 5% for both FAU and diamond.

The phonon dispersions are obtained using the frozen phonon approach with supercell sizes of 3 × 3 × 3 and 6 × 6 × 6 for FAU and diamond. The harmonic force constants are obtained using the finite-difference approach with a step size of 0.005 Å and the interaction cut-off of ~14 Å. Vibrational density of states (DOS) is calculated from the velocity autocorrelation function with 200 correlation steps. The amorphous counterparts of FAU and diamond (named as a-FAU and a-diamond, respectively) are generated using the melt-quench method [18]. For this, the crystalline system is first melted at a temperature of 15000 K for 30 ps, resulting in an extremely disordered structure. Next, the system is cooled to 1000 K with a cooling rate of 100 K/ps followed by annealing for 1 ns. Finally, the system is cooled to 300 K at a rate of 100 K/ps. All temperatures are controlled using the Berendson thermostat along with NVT ensemble. The final structure is obtained by an equilibration run of 2 ns using NVT ensemble to remove high-energy artifacts and reach a stable state (Fig. 1(c)). For the melt-quench method, the coordination cutoff is set at 1.85 Å.

3. Results

We start by first testing the validity of NEP potential for carbon-based systems. For this, we investigated thermal transport in crystalline diamond (100% sp^3 bonds) and graphene (100% sp^2 bonds). For crystalline diamond, we also carried out simulations by using the commonly employed Tersoff potential used to model sp^3 carbon [35].

The phonon dispersions obtained using NEP and Tersoff potentials for crystalline diamond are compared against experimental measurements in Fig. 2(a). As can be seen from the figure, while both potentials are able to capture overall phonon dispersion qualitatively, the Tersoff potential results in stiffened phonon dispersion compared to

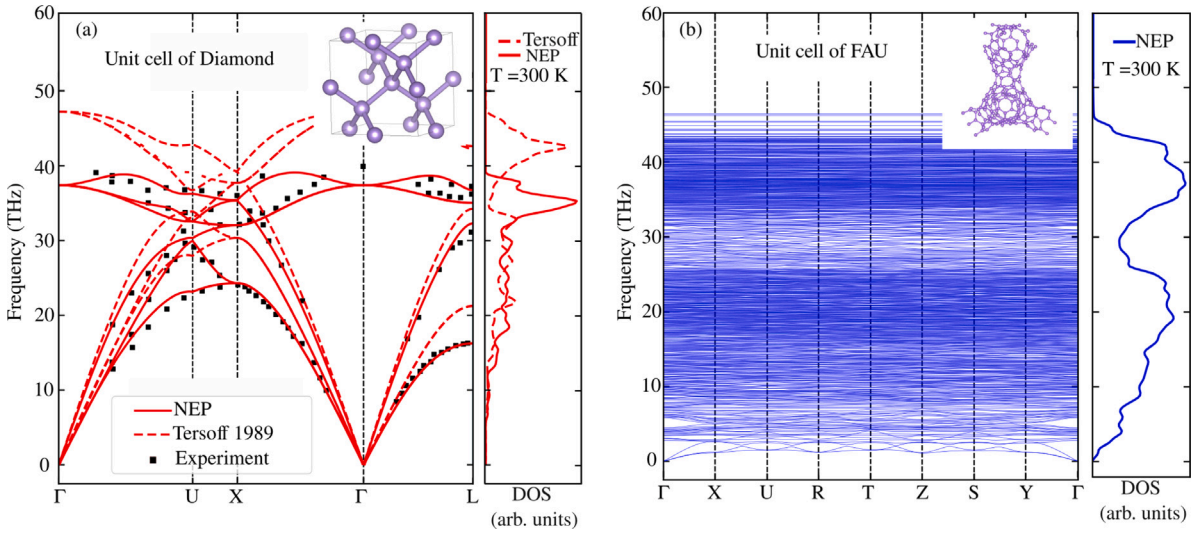

Fig. 2. (a) Phonon dispersion and DOS for diamond; experimental data points are taken from Ref. [36], (b) Phonon dispersion and DOS for FAU, obtained using GPUMD.

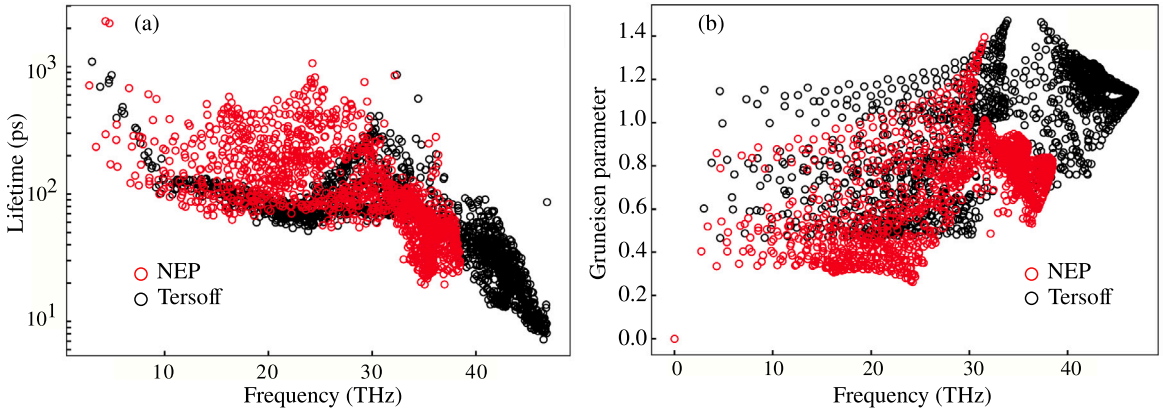

Fig. 3. (a) Phonon lifetimes and (b) Grüneisen parameters for diamond, computed using the BTE-based lattice dynamics approach, with interatomic forces computed Tersoff potential and NEP.

experiments: the obtained sound speed (phonon group velocity of longitudinal acoustic phonons in the long wavelength limit) is 16.3 km/s from the NEP potential compared to 18.7 km/s from the Tersoff potential. With NEP potential, the agreement between experiments and computations is excellent. For instance, at the Γ-point, the computed phonon frequency of the optical phonon is 37.1 THz and 47.4 THz from NEP and Tersoff potential compared to 39.85 THz from experiments.

Next, we calculate the thermal conductivity of crystalline diamond using NEP and Tersoff potentials. We find that even though the Tersoff potential results in stiffer phonons compared to the NEP, the thermal conductivity obtained using Tersoff is 1533 ± 445 W/m-K, compared to more than 2348 ± 926 W/m-K from NEP (the uncertainties are obtained as standard deviations from 25 seeds). To understand this, we compute the phonon relaxation time by considering the three-phonon scattering, using the Boltzmann transport equation (BTE) approach with classical phonon statistics. For this, we used 20 × 20 × 20 phonon wavevector grid and limited the cubic force constants interaction cutoff to 4 Å. As shown in Fig. 3(a), the phonon relaxation times obtained using the Tersoff potential are lower than those from the NEP potential. This is a direct consequence of the stronger anharmonicity of the Tersoff potential, as is reflected in the Grüneissen parameter in Fig. 3(b). The obtained heat capacity weighted mode-averaged Grüneissen parameter is 0.99 using the Tersoff potential, as compared to 0.71 from NEP calculations. We also calculated the thermal conductivity of crystalline diamond using the BTE approach and compared the results obtained from the NEP potential with those from DFT-based forces. We find that at 300 K, the thermal conductivity obtained from the NEP and DFT-based forces is within 5%, thus establishing the validity of the NEP potential in describing thermal transport physics in sp^3 carbon systems. Similarly, we also computed the thermal conductivity of graphene using the NEP potentials and compared them against the DFT-based results. We find that the graphene basal-plane thermal conductivity obtained using the NEP potential and DFT is within 5%, thus validating the NEP potential for studying thermal transport properties of both sp^3- and sp^2-bonded carbon systems.

Moving ahead, we next compute thermal transport properties of FAU and report phonon dispersion in Fig. 2(b) and thermal conductivity in Fig. 4(d). We note that due to a large number of atoms in the unit cell of FAU, it is not possible to compute thermal conductivity via the BTE approach. As such, the thermal conductivity of FAU is obtained using only the EMD approach with the NEP potential. As can be seen from Fig. 2(b), while the phonon dispersion of FAU is much more complex than that of diamond due to 176 atoms in the unit cell, the maximum phonon frequency is similar in FAU and diamond. The speed of sound is much lower in FAU (10.6 km/s) compared to that in diamond (18.7 km/s). Further, the DOS for low-frequency phonons in FAU is much higher than that in diamond, suggesting many possibilities of satisfying phonon scattering selection rules and hence,

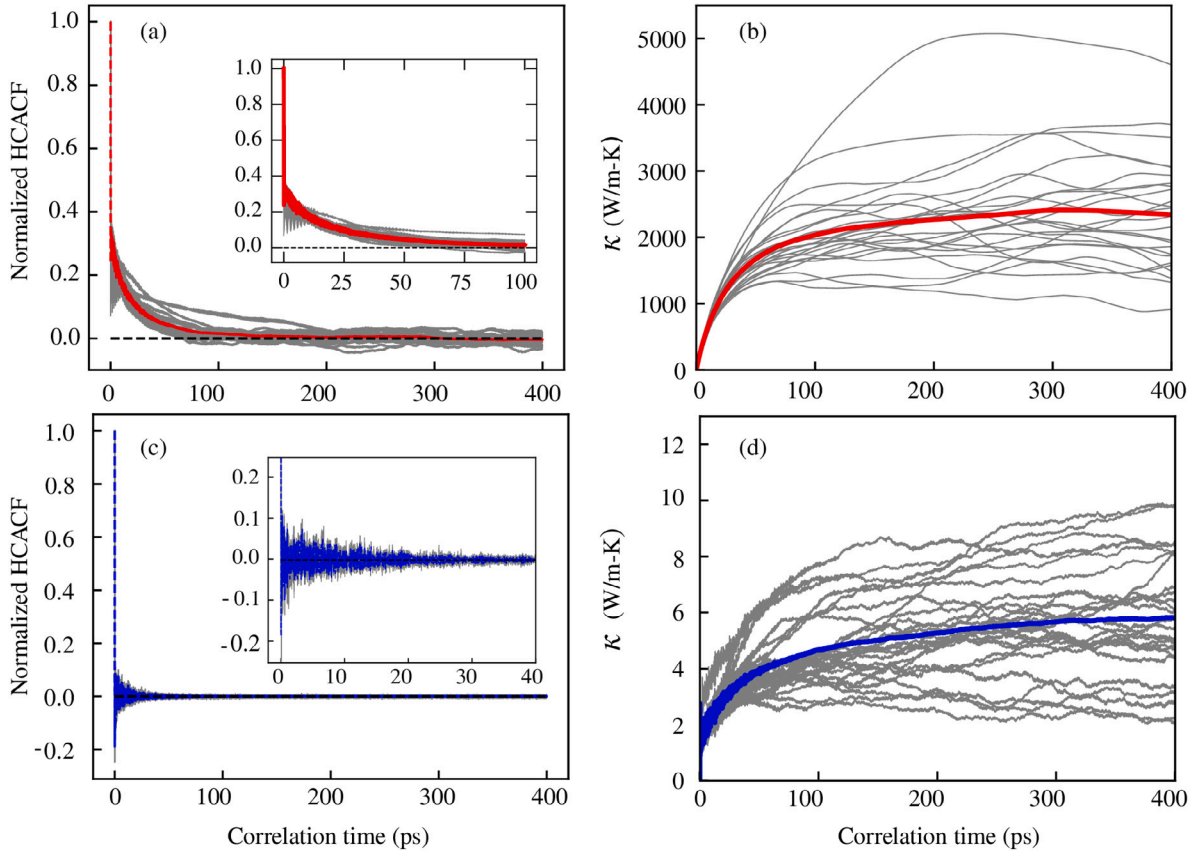

Fig. 4. (a) Normalized HCACF and (b) the corresponding integrated thermal conductivity as a function of correlation time for crystalline diamond. (c) Normalized HCACF and (d) the corresponding integrated thermal conductivity for crystalline FAU. The grey lines represent results from independent random seed simulations, while the solid red and blue lines denote the averages over 25 seeds for diamond and FAU, respectively.

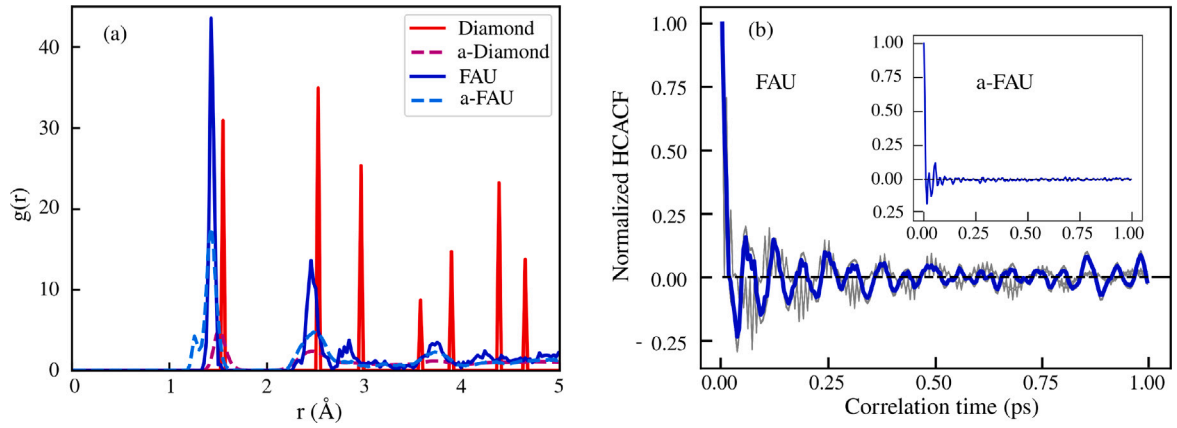

Fig. 5. (a) Radial distribution function g(r) of diamond, FAU, a-diamond and a-FAU (b) HCACF of crystalline FAU (Fig. 4(c)); the inset illustrates the HCACF corresponding to the amorphous FAU structure.

more phonon-phonon scattering in FAU compared to diamond. This is indeed reflected in the thermal conductivity reported in Fig. 4(b,d), where the obtained thermal conductivity of FAU is 5.43 ± 2.12 W/m-K compared to 2348 ± 926 W/m-K for diamond using the same potential. The HCACF for diamond and FAU are presented in Figs. 4(a) and 4(c). For diamond, the HCACF decays monotonically (with small oscillations) to zero around 100 ps, while for FAU, the HCACF has more oscillations and decays quickly to zero before 30 ps. This behaviour of HCACF in FAU is similar to that of amorphous materials [34,37], which is also reflected in the final obtained thermal conductivity of 5.43 ± 2.12 W/m-K, which matches with experimentally reported value for fullerene-derived HC [26] and falls in the range of disordered carbon values. It is worthwhile to note that the direction-averaged mean square displacements in FAU (0.008 Å^2) are higher than those in diamond (0.002 Å^2), suggesting that the thermal conductivity of FAU is lower due to the combined effect of reduced phonon group velocities, stronger anharmonicity, and larger phonon scattering phase space.

To place the thermal conductivity of FAU in context with other carbon allotropes, we compare it with previously reported results obtained using EMD/HNEMD within the GPUMD framework. Graphene exhibits extremely high thermal conductivity of ~2812–2960 W/m-K, while other sp^2 carbon allotropes show comparatively lower values.

For example, pentaheptite and the biphenylene network have reported thermal conductivities of ~342–375 W/m-K and ~208–229 W/m-K, respectively [38]. Likewise, the quasi-tetragonal phase C_{24} monolayer exhibits a thermal conductivity of ~272 W/m-K [39]. In fullerene-based networks, Dong et al. reported thermal conductivity values of ~109 W/m-K (x-direction) and ~138 W/m-K (y-direction) for quasi-hexagonal buckyball framework, whereas bulk phase fullerene is reported to have an ultralow thermal conductivity of ~0.45 W/m-K [40]. The thermal conductivity computed for FAU from our simulations lies within the broader range of values observed across carbon allotropes.

3.1. Disordered FAU and diamond

We next investigate thermal transport in amorphous carbon by converting both FAU and diamond into their amorphous counterparts (a-FAU and a-diamond) and computing their thermal conductivities to examine whether the behaviour observed in the crystalline state is retained in the disorder-dominated regime. The hybridization and radial distribution function (RDF) for a-FAU is presented in Fig. 1(b) and 5(a). Our analysis shows that the pore distribution in a-FAU produces a homogeneous atomic network. In a-FAU, the proportion of sp^2 orbital hybridization decreases to ~75% relative to the crystalline phase, with the remaining ~25% corresponding to sp hybridization (Fig. 1(b)). In contrast, a-diamond exhibits only a minimal change in its bonding configuration, with sp^3 hybridization reduced by just 5% from that of the crystalline structure.

For crystalline diamond, the RDF shows sharp peaks at regular intervals as seen in Fig. 5(a), indicating long-range periodic interactions among atoms. In contrast, crystalline FAU displays reduced peak intensities in the RDF, revealing comparatively weaker short-range interactions. The nearest-neighbour distance in diamond is approximately 1.55 Å, whereas in crystalline FAU it is shorter (~ 1.43 Å), which can be attributed to the presence of sp^2 hybridization. In both a-diamond and a-FAU, the long-range peaks in the RDF either broaden significantly or vanish, reflecting the loss of periodicity and the increase in structural disorder. Notably, beyond the second peak, the RDF of crystalline FAU resembles that of amorphous structures. This indicates a coexistence of short-range crystalline ordering with long-range amorphous-like behaviour, which aligns with its lower thermal conductivity relative to diamond. The computed thermal conductivity of a-diamond at 300 K is 9.8 ± 4.29 W/m-K, which is nearly two orders of magnitude reduction relative to their crystalline counterpart. In our a-diamond sample, the density is 3.53 g/cm^3, and the sp^3 fraction is 95%. Moon et al. reported a thermal conductivity of ~8.52 W/m-K for a-diamond with a density of 3.5 g/cm^3 and 90% sp^3 hybridization, which increases to 10.11 W/m-K when both density and sp^3 concentration are higher [18]. The small difference between our calculated value and the reported data arises primarily from variations in density and sp^3 content.

The thermal conductivity of a-FAU decreases to 1.48 ± 0.50 W/m-K, accompanied by a reduction in sp^2 content to ~75% and increased structural disorder. The RDF of a-FAU confirms the loss of medium- and long-range order beyond the first coordination shell, indicating a transition towards a more amorphous-like network. This increased disorder improves phonon scattering, suppresses phonon group velocities, and shortens effective phonon lifetimes, as reflected by the rapid decay of the HCACF (inset of Fig. 5(b)) compared to crystal FAU. Consequently, thermal transport in HC becomes increasingly dominated by diffusive vibrational modes, similar to a-diamond, despite differences in bonding character and density. These results highlight that in HC, structural disorder and hybridization state jointly govern thermal conductivity, leading to amorphous-like heat transport behaviour even in a nominally crystalline framework.

4. Concluding remarks

In this study, we investigated the thermal transport properties of FAU and the role of structural disorder in the thermal transport properties using molecular dynamics simulations with NEP. We find that being crystalline in nature, the thermal conductivity of FAU lies in the range of thermal conductivity of amorphous carbons as a result of reduced phonon group velocities, stronger anharmonicity, and larger phonon scattering phase space. In addition, the role of structural disorder is confirmed by the RDF and HCACF analysis. Both indicate a clear reduction in thermal conductivity compared to the crystalline counterpart. This reduction arises from the loss of medium- and long-range order in the amorphous structures. The extent of this disorder is further influenced by changes in the hybridization states. Our findings on HC, which is porous and structurally heterogeneous despite being nominally crystalline, are consistent with the broader understanding of heat transport in low-density, disordered carbon.

In general, this work provides a systematic understanding of how structural disorder influences thermal transport in HC and related amorphous carbon structures. The results highlight the role of the bonding configuration and loss of long-range order in governing thermal conductivity. These insights help clarify the thermal behaviour of structurally complex carbon systems and can inform future efforts to optimize carbon-based electrodes for thermal management in battery applications.

CRediT authorship contribution statement

Neha Rajput: Writing – original draft, Visualization, Validation, Methodology, Investigation, Formal analysis, Data curation. **Nidheesh Virakante:** Writing – review & editing, Methodology, Investigation, Formal analysis. **Hardik L. Kagdada:** Writing – review & editing, Methodology, Investigation. **Ankit Jain:** Writing – review & editing, Supervision, Resources, Project administration, Methodology, Investigation, Funding acquisition, Conceptualization.

Declaration of competing interest

The authors declare that they have no known competing financial interests or personal relationships that could have appeared to influence the work reported in this paper.

Acknowledgements

The authors acknowledge financial support from the IRCC, India, IIT Bombay, India. The calculations were carried out on the SpaceTime-II and PARAM rudra supercomputing facilities of IIT Bombay.

Data availability

The input files used in our simulations are available at the following link. Additional data will be made available on request.

FAU_Dataset (Original data) (Mendeley Data)

References

[1] H. Shi, J. Barker, M.Y. Saidi, R. Koksbang, L. Morris, Graphite structure and lithium intercalation, J. Power Sources 68 (2) (1997) 291–295.
[2] Hiroki Moriwake, Akihide Kuwabara, Craig A.J. Fisher, Yuichi Ikuhara, Why is sodium-intercalated graphite unstable?, RSC Adv. 7 (58) (2017) 36550–36554.
[3] Yuqi Li, Yaxiang Lu, Philipp Adelhelm, Maria-Magdalena Titirici, Yong-Sheng Hu, Intercalation chemistry of graphite: alkali metal ions and beyond, Chem. Soc. Rev. 48 (17) (2019) 4655–4687.
[4] Xinwei Dou, Ivana Hasa, Damien Saurel, Christoph Vaalma, Liming Wu, Daniel Buchholz, Dominic Bresser, Shinichi Komaba, Stefano Passerini, Hard carbons for sodium-ion batteries: Structure, analysis, sustainability, and electrochemistry, Mater. Today 23 (2019) 87–104.

[5] Xiaoyang Chen, Nurbiye Sawut, Kean Chen, Hui Li, Jun Zhang, Zhe Wang, Mei Yang, Guo Tang, Xinping Ai, Hanxi Yang, et al., Filling carbon: a microstructure-engineered hard carbon for efficient alkali metal ion storage, Energy & Environ. Sci. 16 (9) (2023) 4041–4053.
[6] Zhenyu Guo, Zhen Xu, Fei Xie, Jinglin Jiang, Kaitian Zheng, Sarat Alabidun, Maria Crespo-Ribadeneyra, Yong-Sheng Hu, Heather Au, Maria-Magdalena Titirici, Investigating the superior performance of hard carbon anodes in sodium-ion compared with lithium-and potassium-ion batteries, Adv. Mater. 35 (42) (2023) 2304091.
[7] Ling-Fei Zhao, Zhe Hu, Wei-Hong Lai, Ying Tao, Jian Peng, Zong-Cheng Miao, Yun-Xiao Wang, Shu-Lei Chou, Hua-Kun Liu, Shi-Xue Dou, Hard carbon anodes: fundamental understanding and commercial perspectives for na-ion batteries beyond li-ion and k-ion counterparts, Adv. Energy Mater. 11 (1) (2021) 2002704.
[8] Yingzhe Gao, Kai Zhang, Xiaohang Du, Guihua Liu, Yawei Du, Jingde Li, Wood-derived closed pore hard carbon encapsulated micro-sized silicon anode design for long-term practical lithium-ion battery, Chem. Eng. J. 508 (2025) 160846.
[9] Yuliang Cao, Lifen Xiao, Maria L Sushko, Wei Wang, Birgit Schwenzer, Jie Xiao, Zimin Nie, Laxmikant V. Saraf, Zhengguo Yang, Jun Liu, Sodium ion insertion in hollow carbon nanowires for battery applications, Nano Lett. 12 (7) (2012) 3783–3787.
[10] Xi-Shuo Wu, Xiao-Ling Dong, Bo-Yang Wang, Ji-Li Xia, Wen-Cui Li, Revealing the sodium storage behavior of biomass-derived hard carbon by using pure lignin and cellulose as model precursors, Renew. Energy 189 (2022) 630–638.
[11] D.G. Onn, A. Witek, Y.Z. Qiu, T.R. Anthony, W.F. Banholzer, Some aspects of the thermal conductivity of isotopically enriched diamond single crystals, Phys. Rev. Lett. 68 (18) (1992) 2806.
[12] Zheyong Fan, Luiz Felipe C. Pereira, Petri Hirvonen, Mikko M. Ervasti, Ken R. Elder, Davide Donadio, Tapio Ala-Nissila, Ari Harju, Thermal conductivity decomposition in two-dimensional materials: Application to graphene, Phys. Rev. B 95 (14) (2017) 144309.
[13] Jia-Hao Xiong, Zi-Jun Qi, Kang Liang, Xiang Sun, Zhan-Peng Sun, Qi-Jun Wang, Li-Wei Chen, Gai Wu, Wei Shen, Molecular dynamics study of thermal conductivities of cubic diamond, lonsdaleite, and nanotwinned diamond via machine-learned potential, Chin. Phys. B 32 (12) (2023) 128101.
[14] Liping Shi, Xiaoliang Ma, Mingwei Li, Yesheng Zhong, Lin Yang, Weilong Yin, Xiaodong He, Molecular dynamics simulation of phonon thermal transport in nanotwinned diamond with a new optimized tersoff potential, Phys. Chem. Chem. Phys. 23 (14) (2021) 8336–8343.
[15] Irene Suarez-Martinez, N.A. Marks, Effect of microstructure on the thermal conductivity of disordered carbon, Appl. Phys. Lett. 99 (3) (2011).
[16] Nan Sheng, Takahiro Nomura, Chunyu Zhu, Hiroki Habazaki, Tomohiro Akiyama, Cotton-derived carbon sponge as support for form-stabilized composite phase change materials with enhanced thermal conductivity, Sol. Energy Mater. Sol. Cells 192 (2019) 8–15.
[17] M. Wiener, G. Reichenauer, F. Hemberger, H.P. Ebert, Thermal conductivity of carbon aerogels as a function of pyrolysis temperature, Int. J. Thermophys. 27 (2006) 1826–1843.
[18] Jaeyun Moon, Zhiting Tian, Crystal-like thermal transport in amorphous carbon, Npj Comput. Mater. 11 (1) (2025) 1–8.
[19] Lei Zhong, Wenli Zhang, Shirong Sun, Lei Zhao, Wenbin Jian, Xing He, Zhenyu Xing, Zixiong Shi, Yanan Chen, Husam N. Alshareef, et al., Engineering of the crystalline lattice of hard carbon anodes toward practical potassium-ion batteries, Adv. Funct. Mater. 33 (8) (2023) 2211872.
[20] Jiaqi Li, Chen Peng, Jie Li, Jingkun Wang, Hongliang Zhang, Insight into sodium storage behaviors in hard carbon by reaxff molecular dynamics simulation, Energy & Fuels 36 (11) (2022) 5937–5952.
[21] Ruiqi Dong, Lumin Zheng, Ying Bai, Qiao Ni, Yu Li, Feng Wu, Haixia Ren, Chuan Wu, Elucidating the mechanism of fast na storage kinetics in ether electrolytes for hard carbon anodes, Adv. Mater. 33 (36) (2021) 2008810.
[22] Hongtao Yu, Zonglin Yi, Wanru Jia, Weiyan Hou, Lijing Xie, Zhenbing Wang, Jingpeng Chen, Fangyuan Su, Dong Jiang, Cheng-Meng Chen, Confinement-induced stability evolution of na clusters in closed pores of hard carbon: A dft and aimd study, J. Phys. Chem. A 2025.
[23] Vilas G. Pol, Jianguo Wen, Kah Chun Lau, Samantha Callear, Daniel T. Bowron, Chi-Kai Lin, Sanket A. Deshmukh, Subramanian Sankaranarayanan, Larry A. Curtiss, William I.F. David, et al., Probing the evolution and morphology of hard carbon spheres, Carbon 68 (2014) 104–111.
[24] Dayton G. Kizzire, Alexander M. Richter, David P. Harper, David J. Keffer, Lithium and sodium ion binding mechanisms and diffusion rates in lignin-based hard carbon models, Acs Omega 6 (30) (2021) 19883–19892.
[25] P. Pavan Kumar, Asutosh Agrawal, Debasis Nayak, Koushik Biswas, Sudipto Ghosh, Tarun Kumar Kundu, A comprehensive diffusion-induced stress coupled multiscale modeling and analysis in hard-carbon electrodes of li-ion batteries, Phys. Chem. Chem. Phys. 25 (30) (2023) 20462–20472.
[26] Ana Smontara, Katica Biljaković, Damir Starešinić, M.E. Kozlov Damir Pajić, M. Hirabayashi, M. Tokumoto, H. Ihara, Thermal conductivity of hard carbon prepared from c60 fulleren, Phys. B 219 (1996) 160–162.
[27] Pawan Boonyoung, Takatoshi Kasukabe, Yasuto Hoshikawa, Ángel Berenguer-Murcia, Bundet Boekfa Diego Cazorla-Amorós, Hirotomo Nishihara, Takashi Kyotani, Khanin Nueangnoraj, A simplenano-templating, method using zeolite y toward the formation of carbon schwarzites, Front. Mater. 6 (2019) 104.
[28] Efrem Braun, Yongjin Lee, Seyed Mohamad Moosavi, Senja Barthel, Rocio Mercado, Igor A. Baburin, Davide M. Proserpio, Berend Smit, Generating carbon schwarzites via zeolite-templating, Proc. Natl. Acad. Sci. 115 (35) (2018) E8116–E8124.
[29] Nicholas P. Stadie, Shutao Wang, Kostiantyn V. Kravchyk, Maksym V. Kovalenko, Zeolite-templated carbon as an ordered microporous electrode for aluminum batteries, ACS Nano 11 (2) (2017) 1911–1919.
[30] Zheyong Fan, Yanzhou Wang, Penghua Ying, Keke Song, Junjie Wang, Yong Wang, Zezhu Zeng, Ke Xu, Eric Lindgren, J. Magnus Rahm, J. Gabourie Alexander, Jiahui Liu, Haikuan Dong, Jianyang Wu, Yue Chen, Zheng Zhong, Jian Sun, Paul Erhart, Yanjing Su, Tapio Ala-Nissila, GPUMD: A package for constructing accurate machine-learned potentials and performing highly efficient atomistic simulations, J. Chem. Phys. 157 (11) (2022) 114801, http://dx.doi.org/10.1063/5.0106617.
[31] Zheyong Fan, Yang Xiao, Yanzhou Wang, Penghua Ying, Shunda Chen, Haikuan Dong, Combining linear-scaling quantum transport and machine-learning molecular dynamics to study thermal and electronic transports in complex materials, J. Phys.: Condens. Matter. 36 (24) (2024) 245901.
[32] Patrick Rowe, Volker L. Deringer, Piero Gasparotto, Gábor Csányi, Angelos Michaelides, An accurate and transferable machine learning potential for carbon, J. Chem. Phys. 153 (3) (2020).
[33] D.A. McQuarrie, Statistical Mechanics University Science Books, 1997.
[34] Alan J.H. McGaughey, Massoud Kaviany, Phonon transport in molecular dynamics simulations: formulation and thermal conductivity prediction, Adv. Heat Transf. 39 (2006) 169–255.
[35] JJPRB Tersoff, Modeling solid-state chemistry: Interatomic potentials for multicomponent systems, Phys. Rev. B 39 (8) (1989) 5566.
[36] P. Pavone, K. Karch, D. Strauch O. Schütt, W. Windl, Paolo Giannozzi, S. Baroni, Ab initio lattice dynamics of diamond, Phys. Rev. B 48 (5) (1993) 3156.
[37] V.A. Luchnikov, N.N. Medvedev, Yu I. Naberukhin, V.N. Novikov, Inhomogeneity of the spatial distribution of vibrational modes in a computer model of amorphous argon, Phys. Rev. B 51 (21) (1995) 15569.
[38] Penghua Ying, Ting Liang, Yao Du, Jin Zhang, Xiaoliang Zeng, Zheng Zhong, Thermal transport in planar sp2-hybridized carbon allotropes: A comparative study of biphenylene network, pentaheptite and graphene, Int. J. Heat Mass Transfer 183 (2022) 122060.
[39] Qing Li, Haikuan Dong, Penghua Ying, Zheyong Fan, Anisotropic and isotropic elasticity and thermal transport in monolayer c24 networks from machine-learning molecular dynamics, Int. J. Heat Mass Transfer 260 (2026) 128505.
[40] Haikuan Dong, Chenyang Cao, Penghua Ying, Zheyong Fan, Ping Qian, Yanjing Su, Anisotropic and high thermal conductivity in monolayer quasi-hexagonal fullerene: A comparative study against bulk phase fullerene, Int. J. Heat Mass Transfer 206 (2023) 123943.